THE JOURNAL OF PHYSICAL CHEMISTRY C

Article

pubs.acs.org/JPCC

Precursor Geometry Determines the Growth Mechanism in Graphene Nanoribbons

Fabian Schulz,[†,‡] Peter H. Jacobse,[‡,§] Filippo Federici Canova,[∥] Joost van der Lit,[§] David Z. Gao,[⊥] Adrianus van den Hoogenband,[#] Patrick Han,[▽] Robertus J.M. Klein Gebbink,[#] Marc-Etienne Moret,[#] Pekka M. Joensuu,[○] Ingmar Swart,[*,§] and Peter Liljeroth[*,†]

[†]Department of Applied Physics, Aalto University School of Science, P.O. Box 15100, 00076 Aalto, Finland

[§]Condensed Matter and Interfaces, Debye Institute for Nanomaterials Science, Utrecht University, P.O. Box 80000, 3508 TA Utrecht, The Netherlands

[∥]Aalto Science Institute, Aalto University, P.O. Box 15500, 00076 Aalto, Finland

[⊥]Department of Physics and Astronomy, University College London, Gower Street, London WC1E 6BT, United Kingdom

[#]Organic Chemistry & Catalysis, Debye Institute for Nanomaterials Science, Utrecht University, Universiteitsweg 99, 3584 CG Utrecht, The Netherlands

[▽]Advanced Institute for Materials Research (AIMR), Tohoku University, Sendai 980-8577, Japan

[○]Department of Chemistry, Aalto University School of Chemical Technology, P.O. Box 16100, Aalto 00076, Finland

S *Supporting Information*

ABSTRACT: On-surface synthesis with molecular precursors has emerged as the de facto route to atomically well-defined graphene nanoribbons (GNRs) with controlled zigzag and armchair edges. On Au(111) and Ag(111) surfaces, the prototypical precursor 10,10′-dibromo-9,9′-bianthryl (DBBA) polymerizes through an Ullmann reaction to form straight GNRs with armchair edges. However, on Cu(111), irrespective of the bianthryl precursor (dibromo-, dichloro-, or halogen-free bianthryl), the Ullmann route is inactive, and instead, identical chiral GNRs are formed. Using atomically resolved noncontact atomic force microscopy (nc-AFM), we studied the growth mechanism in detail. In contrast to the nonplanar BA-derived precursors, planar dibromoperylene (DBP) molecules do form armchair GNRs by Ullmann coupling on Cu(111), as they do on Au(111). These results highlight the role of the substrate, precursor shape, and molecule−molecule interactions as decisive factors in determining the reaction pathway. Our findings establish a new design paradigm for molecular precursors and opens a route to the realization of previously unattainable covalently bonded nanostructures.

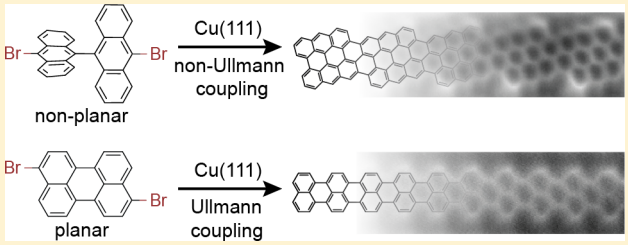

INTRODUCTION

Graphene nanoribbons (GNRs) are narrow, one-dimensional structures derived from two-dimensional graphene. GNRs have been proposed as a means for introducing a tunable band gap into graphene while preserving its favorable electronic properties.[1,2] Such a band gap is a prerequisite to electronic applications of graphene and, together with the predicted spin-polarized flat-band edge states for certain edge terminations, gives GNRs enormous potential for use in next-generation nanoelectronics.[2] As a result, tremendous efforts have been devoted to the top-down fabrication of nanoribbons, for example, through the lithographic etching of graphene[3,4] or the "unzipping" of carbon nanotubes.[5,6] However, using these methods, it is not possible to produce nanoribbons with atomically well-defined edges. As the electronic properties of GNRs are intricately linked to their edge structure,[2,7] methods for synthesizing GNRs with atomically precise widths and edge structures need to be developed for actual applications.

On-surface synthesis has emerged as a complementary approach for obtaining covalently bonded nanostructures.[8] Using suitable precursor molecules, this bottom-up approach yields atomically well-defined graphene nanoribbons with either the armchair[9] or zigzag[10] edge topology. The beauty of this approach is that, by changing the precursor molecule, the resulting nanoribbon structure can be precisely selected. Since the initial demonstration of seven-atom-wide armchair GNRs (7-AGNRs) synthesized by coupling 10,10′-dibromo-9,9′-bianthryl (DBBA, **1**) on a Au(111) surface,[9] the field has progressed rapidly. Addition of biphenyl and (thiophenyl)-phenyl moieties to DBBA molecules results in the formation of 13-AGNRs[11] and sulfur-doped GNRs,[12] respectively, whereas incorporation of a diboraanthracene moiety into the molecule

Received: December 9, 2016
Revised: January 10, 2017
Published: January 11, 2017

DOI: 10.1021/acs.jpcc.6b12428
J. Phys. Chem. C 2017, 121, 2896−2904

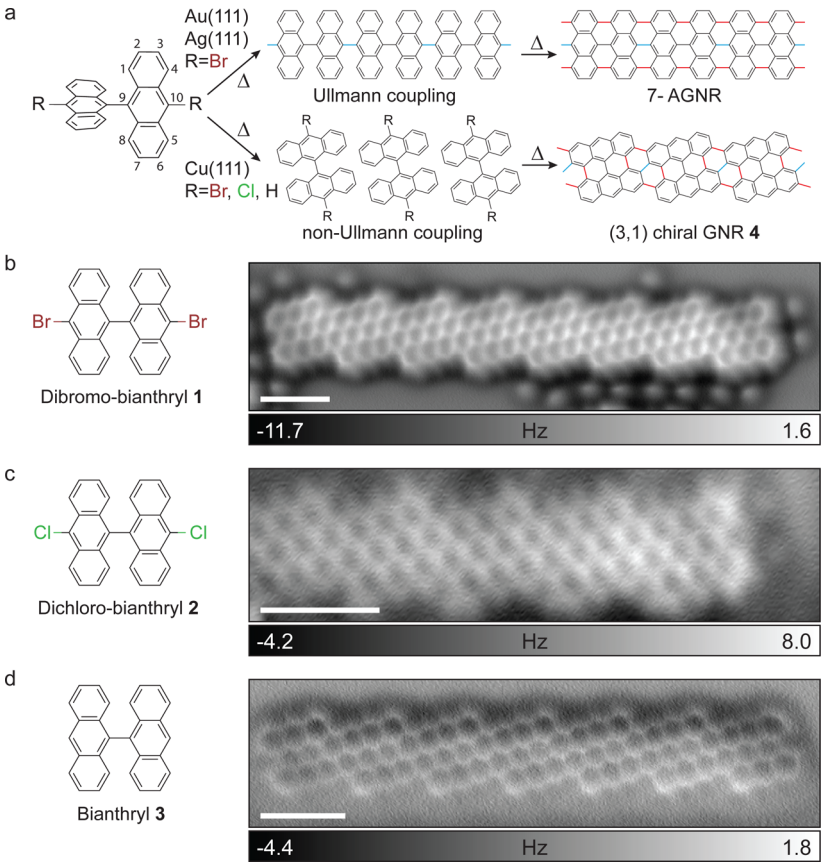

Figure 1. Synthesis of chiral graphene nanoribbons on Cu(111) from different bianthryl precursors. (a) Three-dimensional wireframe representation of the bianthryl precursor with different functionalizations (R = Br, Cl, or H) and two-dimensional schematics of the molecular coupling on Au(111) and Ag(111) (top, following Ullmann coupling) and on Cu(111) resulting in the observed (3,1) chiral nanoribbons (bottom). Bonds in red result from intramolecular cyclodehydrogenation, and those in blue result from intermolecular aryl−aryl coupling. (b−d) Two-dimensional wireframe representations of the precursor and nc-AFM images of the resulting nanoribbons for (b) DBBA/Cu(111) annealed to 620 K, (c) DCBA/Cu(111) annealed to 550 K, and (d) BA/Cu(111) annealed to 510 K. All scale bars represent 1 nm.

allows for the synthesis of boron-doped 7-AGNRs.[13,14] The versatility of the bottom-up method is further illustrated by the numerous examples of GNRs that have been established recently, such as chevron-type GNRs[9] and their nitrogen-doped counterparts,[15,16] ultranarrow 5-AGNRs,[17,18] and zigzag GNRs with modified edges.[10,19,20]

Typically, the synthesis is carried out on gold (occasionally silver[21]) substrates, and it has been proposed to proceed through the metal-catalyzed Ullmann coupling of aryl halides.[8,22,23] The reaction mechanism is not completely known, but the first step involves metal-substrate-catalyzed cleavage of the carbon−halogen bond, resulting in a radical species,[24] followed by aryl−aryl coupling to form polymer chains (protoribbons) at elevated temperatures. These protoribbons are converted to fully aromatic GNRs through cyclodehydrogenation at an even higher temperature (Figure 1a).[9,23]

It would be of interest to extend GNR synthesis to the technologically more relevant copper surfaces, for which large-scale graphene growth and reliable transfer techniques have been developed with great success in recent years.[25−27] Simonov et al.[28] described the synthesis of GNRs on Cu(111) from DBBA precursors. Based on the earlier experiments on Au(111) and Ag(111)[9,21] and the assumption that the molecules follow the same Ullmann-coupling mechanism on Cu(111), the resulting structures were assigned to be 7-AGNRs. However, when the same experiments were performed by Han et al.,[29] a characteristic corrugation of the nanoribbon edges was observed, which was ascribed to the formation of (3,1) chiral GNRs (Figure 1a). The controversy over the actual structure of these ribbons on Cu(111)[30−34] shows the difficulties in assessing the atomic structures of synthesis products by scanning tunneling microscopy (STM). Structure identification by STM is limited, as STM is sensitive to only electronic states near the Fermi energy,[35] which, for polyaromatic hydrocarbons, are usually highly delocalized. A possible solution is offered by frequency-modulation non-contact atomic force microscopy (nc-AFM):[36] nc-AFM images acquired with a passivated tip (e.g., after deliberate attachment of a carbon monoxide molecule) provide a means of visualizing the chemical structure of single molecules,[37] including graphene nanoribbons.[38,39]

In this work, we used atomically resolved nc-AFM images to confirm that DBBA forms (3,1) chiral GNRs on Cu(111) surfaces, in stark contrast to the results obtained on Au(111)[9] and Ag(111),[21] as suggested by Han et al.[29] and verified by Sánchez-Sánchez et al.[34] This implies that the polymerization on Cu(111) does not proceed by the Ullmann coupling route as on Au(111). To establish the reaction mechanism and determine the factors governing it, we repeated the experiments with chlorinated (dichlorobianthryl) and halogen-free (bianthryl) precursors. The nc-AFM images revealed that, in all cases,

DOI: 10.1021/acs.jpcc.6b12428
J. Phys. Chem. C 2017, 121, 2896−2904

the same (3,1) chiral GNRs were formed. We investigated the reaction mechanism with further nc-AFM/STM experiments and followed the evolution of the reaction products from self-assembled molecular chains to linear polymers and eventually to fully aromatic graphene nanoribbons upon controlled annealing to higher temperatures. The importance of molecule−molecule interactions is highlighted by experiments with flat precursors (dibromoperylene, DBP)[17] that do form armchair GNRs on Cu(111) through Ullmann coupling. Our findings suggest a new paradigm for the synthesis of graphene nanoribbons in which the coupling of the precursor molecules is controlled by their geometry rather than their chemical functionality. This break from prototypical Ullmann coupling will allow for the realization of previously unattainable covalently bonded nanostructures.

EXPERIMENTAL METHODS

Sample Preparation. 10,10′-Dibromo-9,9′-bianthryl was synthesized according to the method reported in ref 38, 9,9′-bianthryl and 10,10′-dichloro-9,9′-bianthryl according to the method reported in ref 40, and 3,9-dibromoperylene and 3,10-dibromoperylene according to the method reported in ref 17. The two isomers of dibromoperylene form in a roughly 1:1 ratio during the synthesis for symmetry reasons. Although the isomers could be separated with some effort, the publication of Kimouche et al.[17] showed that the mixture of the two isomers does not seem to affect the GNR formation, as straight GNRs are obtained.

Samples were prepared by evaporating the precursor molecules from Knudsen-cell-type evaporators onto Cu(111) single crystals, cleaned by sputtering/annealing cycles. Low-temperature evaporation for DBBA and DBP was performed by removing the cold Cu substrate from the STM/AFM instrument (∼5 K), positioning it for short time in front of the evaporator, and inserting it immediately back into the STM/AFM instrument. The total time outside the cold microscope was between 2 and 3 min, yielding a conservative estimated temperature (and error margin) of (200 ± 50) K. Thus, the difference in debromination after low-temperature evaporation between DBBA and DBP (see below) is more likely to reflect the variation in sample temperature than different energy barriers for C−Br bond cleavage.

For the experiments on DBBA and DBP, annealing temperatures were monitored using a pyrometer, which is sensitive to the optical alignment with the sample, the way it is calibrated, and potential stray light. For the experiments on DCBA and BA, sample temperatures during annealing were deduced from the filament power and a calibration curve recorded with a pyrometer. A reasonable error estimation for the temperatures reported in this article is ±30 K for each setup. Comparing absolute sample temperatures between different ultrahigh-vacuum systems is generally difficult. While temperature measurements are repeatable as such, large systematic differences between different setups can easily exist.

Scanning Probe Measurements. After preparation, the sample was inserted into a low-temperature STM/AFM instrument, housed within the same ultrahigh-vacuum system (base pressure ≈ 10^{-10} mbar). The experiments on DBBA and DBP precursors were carried out with a Createc LT-STM/AFM system (with a qPlus sensor resonance frequency f_0 of ∼30.7 kHz, a quality factor of ∼100k, a spring constant k of ∼1.8 kN/m, and an oscillation amplitude of 50 pm). The experiments on DCBA and BA precursors were carried out with an Omicron LT-STM/qPlus AFM system (with a qPlus sensor resonance frequency f_0 of ∼19.5 kHz, a quality factor of ∼30k, a spring constant k of ∼1.8 kN/m, and an oscillation amplitude of 85 pm).

Carbon monoxide for nc-AFM imaging with functionalized tips was dosed onto the surface through a leak valve. Picking up an individual carbon monoxide molecule on the tip apex was carried out as described previously.[37,41] nc-AFM images were acquired at a bias voltage (V_{bias}) of 0 V.

THEORETICAL METHODS

DFT Calculations. Density functional theory (DFT) simulations to examine the adsorption geometries and interactions between molecules on the surface were performed with the CP2K code using the Perdew−Burke−Ernzerhof (PBE) generalized gradient approximation (GGA) density functional and a mixed Gaussian and plane wave (GPW) basis set.[42,43] These calculations included geometry minimizations of various molecular variants on the surface. The Cu(111) surface was represented using three atomic layers; the lowermost layer was fixed, whereas the other two layers were allowed to relax to reproduce the atomic and electronic structure of the system. We employed semiempirical long-range dispersion corrections[44] to represent van der Waals (vdW) interactions in the system. Finally, the molecularly optimized (MOLOPT)[45] basis set was used to minimize basis set superposition error (BSSE), and the plane-wave cutoff was selected to be 400 Ry, as, above this value, the results did not change. The lowest-energy configuration of each molecule was computed by placing the molecule onto the surface in various positions and optimizing the geometry. The starting positions were obtained by rotating the molecule by 2° increments on the surface.

nc-AFM Simulations. AFM simulations were performed with the MechAFM code, based on the probe particle model,[46,47] as implemented by Spijker and co-workers.[48] The probe consists of a fixed C atom connected to an O atom restrained in the xy plane by a harmonic spring with a stiffness of 0.5 N/m. The tip−sample interactions were calculated by placing the tip in several locations above the DFT-optimized structures of the molecules and relaxing the tip O termination. For simplicity, the interatomic interactions between O and the atomic species of the sample were described by Lennard-Jones potentials. At this stage, electrostatic interactions were disregarded. The atomic parameters for the potentials were taken from the CHARMM force field[49] (Table 1).

Table 1. CHARMM Force Field Parameters Used in the AFM Image Simulations

element	ϵ (kcal/mol)	σ (Å)
C	0.07	3.55
H	0.03	2.42
Br	0.42	3.69
O (tip)	0.192	3.15

Parameters for pair potentials were obtained from the atomic parameters using arithmetic mixing rules. Frequency shift images were calculated from the tip−sample interaction maps using the method described in ref 50, assuming that the AFM cantilever had a stiffness of 1.8 kN/m and an oscillation amplitude of 50 pm at a resonance frequency of 25 kHz.

DOI: 10.1021/acs.jpcc.6b12428
J. Phys. Chem. C 2017, 121, 2896−2904

RESULTS AND DISCUSSION

We begin by confirming that DBBA (**1**) on Cu(111) forms (3,1) chiral GNRs, as proposed by Han et al.[29] and recently verified by Sánchez-Sánchez et al.[34] Figure 1b shows an nc-AFM constant-height image of a GNR obtained after annealing submonolayer coverages of **1** on Cu(111) to 620 K. The image shows the chemical structure of the GNR and clearly reveals its chiral symmetry, with a periodic arrangement of three zigzag units and one armchair unit comprising the GNR edge. We observed only these chiral GNRs on Cu(111), implying that the formation does not proceed by Ullmann coupling. The general coupling scheme resulting in such ribbons is outlined in Figure 1a.

Surprisingly, the same chiral GNRs can also be synthesized from 10,10′-dichloro-9,9′-bianthryl (DCBA, **2**; Figure 1c), that is, when the bromines in the precursor molecule are replaced by chlorines, and by 9,9′-bianthryl (BA, **3**; Figure 1d), which does not contain any halogen atoms thought to be required for Ullmann-type couplings. Compounds **1** and **3** represent extreme cases, where the radical is expected to form either at the very beginning of the GNR formation process (**1**) or not all (**3**). Because of the C−Cl bond in **2** is stronger than the C−Br bond in **1**,[40,51,52] the radical is formed at a higher temperature, that is, at a later stage in the reaction. Yet the outcome is the same covalently bonded nanostructure with all of the precursors. This confirms that the aryl−aryl coupling is of a non-Ullmann type and suggests that the entire GNR formation is insensitive to radical formation by dehalogenation.

We unravel the chemical mechanism behind the deviation from Ullmann coupling[29,33] and explain why this synthesis proceeds even without aryl halides by performing the synthesis step by step, for all three precursors. Figure 2a shows an STM image of a single DBBA molecule after evaporation onto Cu(111) at (200 ± 50) K, which results in mostly isolated molecules and dimers. The molecule shows the typical dumbbell-like protrusions due to the nonplanar geometry of the bianthryl core, caused by steric hindrance between the inner hydrogen atoms at C1, C1′ and C8, C8′ (Figure 1a). Constant-height nc-AFM images of the same molecule, recorded at different tip−sample distances, are depicted in Figure 2c. When the tip is far away, the molecule is imaged as two repulsive arcs. Because their positions coincide with the two lobes in the STM images, we assign them to the edges of the topmost carbon ring of each of the two anthracene units of DBBA. The tilting of the CO at the tip apex significantly influences the image contrast at closer distances.[46,47] This results in a sharp line diagonally through the center of the molecule and unrelated to any actual bond in the molecule.[53] This feature can be identified based on simulated nc-AFM images including the effect of CO flexibility through a molecular-mechanics model of the tip−sample junction[35,47] with the DFT-optimized geometry of the molecule on the surface. We calculated the adsorption configuration for both the intact DBBA molecule and the debrominated biradical. Upon adsorption on Cu(111), the nonplanar shape of the bianthryl core in both cases is mostly conserved, although the symmetry in comparison to the gas phase is reduced. The two carbon rings closest to the copper tend to adsorb flat on the surface, inducing considerable distortion in the anthracene moieties. In the case of the biradical (Figure 2b), the debrominated C10 and C10′ bend down toward the copper substrate, causing additional strain. Our subsequent nc-AFM simulations reproduced the filament-like feature appearing at small tip−sample distances for both species. This feature is due to the CO bending as a response to a saddle point in the potential energy surface over the molecule,[35] thereby connecting the two upper benzene rings of the two anthracene units. However, the arc-like features at large tip−sample distances were reproduced only in the nc-AFM simulation of the biradical shown in Figure 2d (see Figure S1 for DFT adsorption structure and simulated nc-AFM images of intact DBBA). This is in agreement with the earlier experiments, suggesting that bromine−carbon bond cleavage occurs already below room temperature.[32]

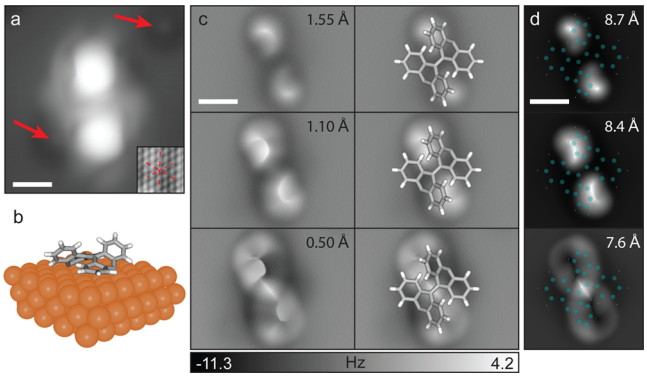

Figure 2. Characterization of the DBBA precursor molecule. (a) STM image of an individual DBBA molecule evaporated onto Cu(111) below room temperature. Red arrows mark adsorbed CO molecules. Inset: Atomically resolved STM image of the Cu(111) substrate. (b) Adsorption configuration for debrominated DBBA as calculated by DFT. (c) Constant-height nc-AFM images at different tip−sample distances, given as offsets with respect to the tunneling set point (left) and overlaid with a structural model of debrominated DBBA (right). (d) Simulated nc-AFM images based on the DFT-optimized geometry. Tip heights are given as distances between the CO carbon atom and the plane of the topmost copper layer. All scale bars represent 5 Å.

As a next step, we heated the DBBA/Cu(111) system to room temperature, giving the results shown in Figure S2a. The molecules self-assemble into wiggly, disordered chain structures with rare and only short straight sections with periodicities between 10 and 11 Å (Figure S2c). STM images with a CO tip reveal cleaved bromine atoms next to the chains (Figure S2b). This assignment is supported by the asymmetric appearance of some of the molecules, likely caused by the scission of only one of the two C−Br bonds of DBBA or asymmetric subsequent stabilization/passivation of the radical. The nc-AFM image shown in Figure S2d suggests that the structure does not deviate significantly from what would be expected for an Ullmann pathway, with the radical sites of adjacent monomers pointing toward each other. Although this cannot be directly verified from the STM or nc-AFM images, the distance between the monomers agrees with the incorporation of copper atoms into the chains, which could stabilize the bianthryl radicals.[30]

Figure 3a presents an STM image of the DBBA/Cu(111) sample after it had been annealed to 470 K. The wiggly, disordered structures have transformed into long, straight molecular chains. Interestingly, the periodicity of the chains is also reduced to about 8.5−9 Å, as confirmed by the STM line profile in Figure 3b. Such a reduction in periodicity was observed previously and was interpreted as a transition from an organometallic chain of surface-stabilized radicals to a polymer.[30] We obtained analogous molecular chains for

DOI: 10.1021/acs.jpcc.6b12428
J. Phys. Chem. C 2017, 121, 2896−2904

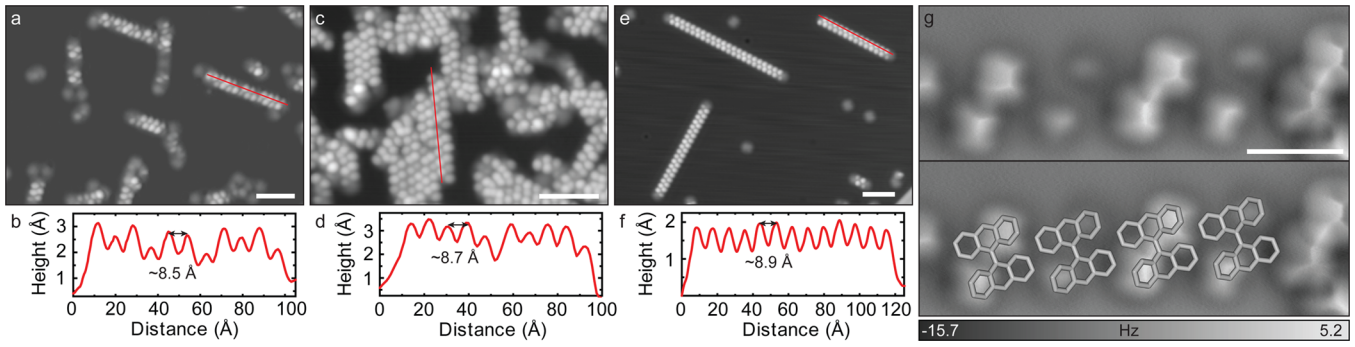

Figure 3. Formation of molecular chains. (a–f) STM images and line profiles of molecular chains formed after annealing (a,b) DBBA/Cu(111) to 470 K, (c,d) DCBA/Cu(111) to 500 K, and (e,f) BA/Cu(111) to 440 K. Scale bars represent 5 nm. (g) nc-AFM image with overlaid structural models (only BA core for clarity) for a chain with short periodicity formed from DBBA precursors. Scale bar represents 1 nm.

DCBA and BA after they had been annealed to 500 and 440 K, respectively, with similar periodicities between 8.5 and 9 Å, as shown in Figure 3c–f. Within the experimental uncertainty, these values are identical to the periodicity of the final (3,1) chiral ribbons of ∼9 Å calculated from purely geometrical considerations. Interestingly, we observed chains with long periodicity for neither DCBA nor BA, despite testing a wide range of annealing temperatures [see Figure S3 for DCBA/Cu(111) and BA/Cu(111) at room temperature].

Within the chains shown in Figure 3, some monomers exhibit a greatly reduced apparent height in the STM images, which is an indication of the onset of cyclodehydrogenation of the bianthryl cores. Indeed, the STM images in Figure 3a,c,e also show individual molecules that are already fully cyclodehydrogenated, similarly to many of the chain ends. The energy barrier for cyclodehydrogenation seems to be considerably higher for molecules within the chains. This might be due to the intermolecular interactions favoring a three-dimensional shape of the bianthryl core or the fact that the cyclodehydrogenation reaction in the middle of a chain would involve the formation of more bonds than that at the chain end. Figure 3g shows an nc-AFM image of a DBBA chain with short periodicity. Even though not all monomers look alike because of the partial cyclodehydrogenation, we used the filament-like feature exhibited by some of them to obtain their orientation. Assuming that the remaining monomers have comparable positions, we found a structure that is radically different from that of the chains with longer periodicity. Instead, it is very close to the orientation of the monomers in the final (3,1) chiral GNRs (see Figure 1a), with the C10 and C10′ sites pointing away from each other and toward the sites of the chain.

The question arises whether the molecules in these chains are already polymerized, which we addressed by STM lateral manipulation experiments.[54] Figure 4a shows a sequence of four STM images. The topmost depicts a straight BA chain, whereas the other three were recorded after subsequent manipulation attempts, in which the tip was positioned on one side of the chain, the tip–sample distance was reduced, and the tip was moved across the chain. As can be seen, the chain did not break, nor were individual molecules extracted. Instead, the chain bent in the direction of tip movement while remaining connected. This is a clear indication that intermolecular bonds have been established at this point of the growth process.[33] These chains are thus the chiral analogues of the so-called protoribbons (polymer chains with a single chemical bond between the monomers) formed on

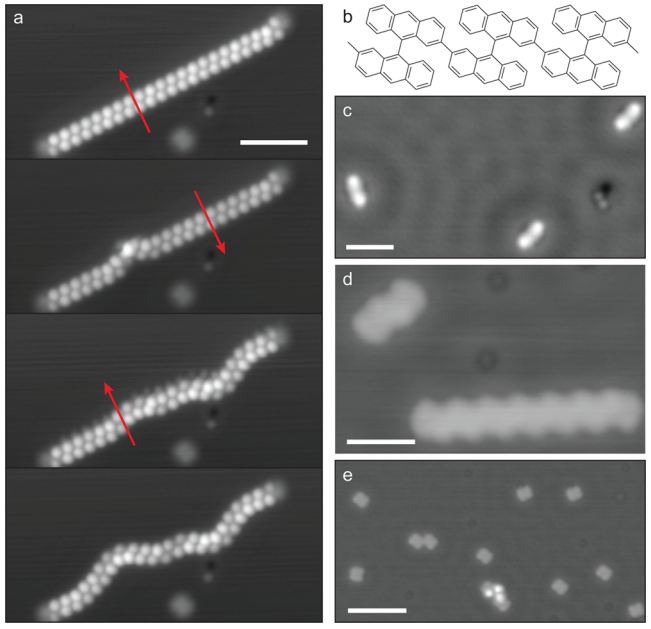

Figure 4. Chain manipulation and quenching of GNR formation by cyclodehydrogenation. (a) Stepwise STM lateral manipulation of a BA chain, starting from the topmost image. Scale bar represents 5 nm. (b) Schematic of a protoribbon in which a single bond connects the BA monomers. (c) STM image of BA molecules evaporated onto Cu(111) at room temperature. Scale bar represents 2 nm. (d) STM image of chiral GNRs formed after the sample in panel c had been annealed to 510 K. Scale bar represents 2 nm. (e) STM image of cyclodehydrogenated BA molecules after evaporation onto a Cu sample held at 510 K. Scale bar represents 5 nm.

Au(111) and Ag(111).[9] Considering the AFM image in Figure 3g, the most likely covalent bond formation is through C2–C2′ coupling, as depicted in Figure 4b. For the DBBA and DCBA precursors, this could be explained by radical hopping from C10 (C10′) to C2 (C2′). However, in the case of BA, no halogen–carbon bond can be cleaved to give rise to a radical. Thus, the unusual C2–C2′ bond formation is most likely due to activation of the corresponding C–H bonds by the catalytic activity of the Cu(111) surface, followed by polymerization into the chains shown in Figure 3 through homocoupling. Formation of these protoribbons subsequently facilitates the ring-closure reaction by cyclodehydrogenation, which is the final step to achieve graphene nanoribbons. Indeed, further annealing leads to the chiral GNRs shown in Figure 1.

DOI: 10.1021/acs.jpcc.6b12428
J. Phys. Chem. C 2017, 121, 2896–2904

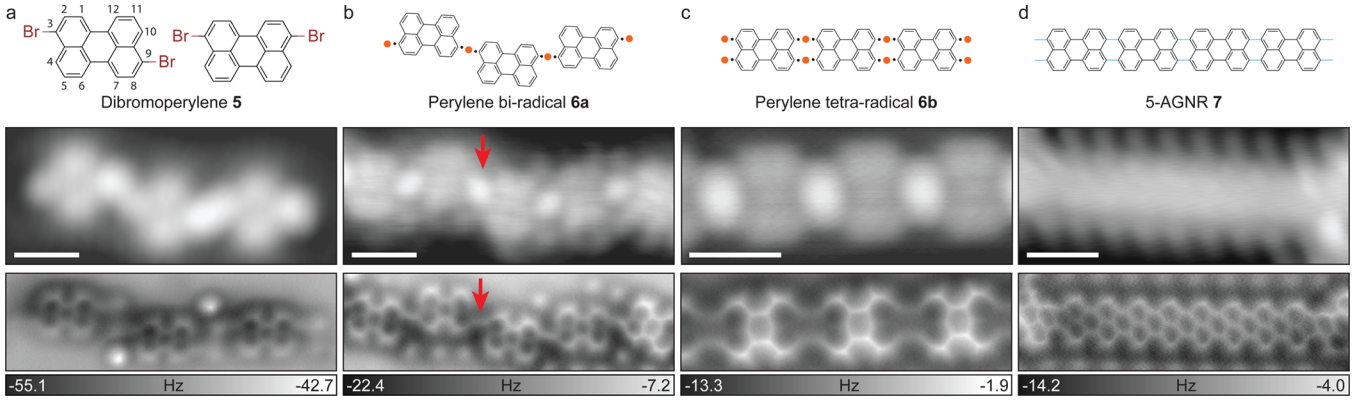

Figure 5. Formation of armchair GNRs from dibromoperylene through on-surface Ullmann coupling on Cu(111). (a–d) Structural model, STM image, and AFM image of DBP evaporated onto Cu(111) at (a) 200 K and (b) room temperature and of DBP on Cu(111) annealed to (c) 470 and (d) 570 K. The two very bright protrusions in the AFM image in panel a are CO molecules. All scale bars represent 1 nm.

The importance of the nonplanar shape of the precursor molecules is emphasized by another set of experiments, depicted in Figure 4c–e. The STM image in panel c shows BA molecules evaporated onto Cu(111) at room temperature, exhibiting their typical dumbbell shape. Figure 4d shows the same sample after it had been annealed to 510 K, resulting in the formation of chiral ribbons. The same evaporation procedure as in panel c was repeated for the sample shown in Figure 4e, except that the Cu(111) substrate was already held at 510 K during the evaporation. As can be seen, no GNRs formed, but the surface is covered by cyclodehydrogenated BA molecules, namely, bisanthenes. Because they were evaporated onto the hot copper surface, the BA molecules cyclodehydrogenated immediately, before they could diffuse around to self-assemble into chains and polymerize, thus efficiently quenching GNR formation.

Thus far, we have established that the surface (Cu vs Au and Ag) has a significant influence on the coupling mechanism. In the following discussion, we further describe how the molecular shape (planar vs nonplanar) affects GNR formation. In Figure 5, we follow, step by step, the GNR formation from planar 3,9-dibromoperylene and 3,10-dibromoperylene (DBP, **5**) precursors[17] on Cu(111), in a manner similar to that described above for the different BA-derived precursors. Figure 5a shows a schematic of DBP and an STM image and the corresponding nc-AFM image of DBP evaporated onto Cu(111) at (200 ± 50) K. Three DBP molecules have assembled into a trimer with the bromines most likely still attached to the perylene core. In contrast, when evaporated onto the Cu(111) sample held at room temperature (Figure 5b), the molecules form long, wiggly chains (see Figure S4 for the STM overview images). Additional circular protrusions are visible next to the chain in both the STM and nc-AFM images, corresponding to the bromines from cleaved carbon-halogen bonds. The nc-AFM image at first suggests the formation of covalent bonds between C3 and C9′ (C10′) of adjacent perylene units (where primed and unprimed carbon atoms indicate the two different perylene units), that is, between radical sites formed by C–Br bond cleavage. However, closer inspection reveals that these apparent bonds have lengths of about 3–4 Å, much too long for a covalent carbon–carbon bond. In addition, the STM image shows bright, circular protrusions at the positions of the perylene–perylene links (indicated by the arrows in Figure 5b). These is likely caused by the inclusion of individual copper atoms into the structure,[18,55] indicating the formation of organometallic chains to stabilize the perylene biradicals (**6a**) after C–Br bond scisson. The exact nature of the copper atoms cannot be identified from our experiments, with both adatoms and surface atoms pulled out of the plane of the top layer of the substrate being plausible.

Figure 5c shows the sample after it had been annealed to 470 K. The appearance of the chains has changed markedly, as they have become straighter and shorter. An analysis similar to that applied to the wiggly chains can be carried out: The apparent bonds in the nc-AFM image between C3 (C4) and C10′ (C9′) of adjacent perylene units are too long for covalent carbon–carbon bonds, and the STM image shows an oblong bright feature at the same position. Because the four carbon atoms C3, C4, C9, and C10 all look alike in the nc-AFM image, with reduced intensity indicating a slight downward bending, we conclude that these features indicate the formation of perylene tetraradicals (**6b**) due to C–H activation, stabilized through formation of organometallic chains connected by copper-atom dimers. We completed the formation of the GNRs by further annealing the sample to 570 K, as highlighted in Figure 5c. The obtained ribbon is a five-atom-wide armchair GNR (5-AGNR), undoubtedly formed by an on-surface Ullmann coupling reaction and thus identical to the results for DBP on Au(111).[17] This confirms that radical coupling is effective in the case of the DBP precursor and points to the nonplanar molecular geometry being responsible for the departure from the Ullmann coupling scheme in the case of the BA-derived precursor molecules.

When performing such a step-by-step synthesis, it is important to differentiate between actual reaction intermediates and self-assembled structures formed upon cooling to the imaging temperature after the heating step. The two types of organometallic chains formed by DBP at different temperatures and the long-periodicity DBBA chains probably represent the latter. Nevertheless, these structures yield important information about the sequence of the different steps along the reaction path. The formation of the perylene tetraradicals indicates that, on Cu(111), the energy barrier for C–H bond activation at C4 and C10 (C9) is significantly lower than that for aryl–aryl homocoupling between C3 and C9′ (C10′), in stark contrast to Au(111), where aryl–aryl coupling precedes C–H bond activation and cyclodehydrogenation.[9,17,56] This also explains the reduced quality of the 5-AGNRs on Cu(111) (Figure S4c): The higher number of radical sites compared to Au(111)

DOI: 10.1021/acs.jpcc.6b12428
J. Phys. Chem. C 2017, 121, 2896–2904

increases the coupling rate and reduces the diffusion rate, which leads to less-ordered structures.[57]

Applying these findings to the chiral ribbons completes our picture of their unusual formation mechanism: Initially, radicals are formed at C10 and C10′ by dehalogenation in the case of DBBA, which form long-periodicity organometallic chains after cooling. Such chains are not observed for DCBA and BA, indicating that dechloronation occurs at similar temperatures as homocoupling or cyclodehydrogenation. The next step occurs analogously for all three precursors, which is C−H activation at the C2 atoms. On Cu(111), this process has a reduced energy barrier compared to that on Au(111), allowing for deviaton from the Ullmann route through C2−C2′ homocoupling. This step is likely driven by $\pi-\pi$ interactions, which can significantly influence adsorption structures[58] and would favor an arrangement of the bianthryl cores in which the C2 and C2′ radical sites point toward each other because of the three-dimensional shape of the precursors.[29] Potential passivation of the C10 and C10′ radical sites for DBBA and DCBA could also facilitate this step. Once the covalent bond between the monomers is established, further heating induces the cyclodehydrogenation of the remaining bianthryl core to form the fully aromatic chiral ribbon.

CONCLUSIONS

Using STM and atomically resolved nc-AFM imaging, we have followed the synthesis of chiral GNRs on Cu(111) from three different BA-derived precursors step by step. Despite radical formation through dehalogenation of the DBBA precursors, the formation of armchair nanoribbons through Ullmann coupling does not occur. This is due to the stronger interaction of the molecule with the surface on Cu(111), which stabilizes the radical after halogen−carbon bond scission and reduces the energy barrier for C−H bond activation. Consequently, C−H bond activation at C2 and C2′ atoms occurs at a lower temperature than C10−C10′ aryl−aryl coupling, resulting in similar intermolecular carbon−carbon bond formation for DBBA, DCBA, and BA. The ring-closure reaction through cyclodehydrogenation yields as the final product the fully aromatic chiral GNR.

The situation is quite different for the planar DBP precursor. Although the observed organometallic chains show that the formed radicals are stabilized by interaction with native substrate atoms, further C−H bond activation and intermolecular carbon−carbon bond formation still results in armchair GNRs. The main difference between these two cases is the three-dimensional shape of the BA-derived precursors that favors molecular chains along the chiral direction. On the fairly inert Au(111) surface, the C−H bond activation at the C2 and C2′ atoms occurs only in the final cyclodehydrogenation step, the difference in the precursor shape is insignificant, and both DBBA and DBP follow the Ullmann coupling pathway. On Cu(111), however, the strong interaction of the precursors with the surface decisively influences the reaction pathway and results in GNR formation being controlled by the precursor shape rather than by the chemical functional groups. This opens up new possibilities for on-surface synthesis in which the precursor shape determines the coupling reaction, thus allowing for the realization of previously unattainable covalently bonded nanostructures.

ASSOCIATED CONTENT

Supporting Information

The Supporting Information is available free of charge on the ACS Publications website at DOI: 10.1021/acs.jpcc.6b12428.

Comparison of DFT adsorption structure and nc-AFM simulation between intact DBBA and the debrominated biradical, DBBA on Cu(111) after annealing to room temperature, BA and DCBA after evaporation onto Cu(111) at room temperature, and STM overview images of the different steps of 5-AGNR formation from DBP on Cu(111) (PDF)

AUTHOR INFORMATION

Corresponding Authors

*E-mail: i.swart@uu.nl.

*E-mail: peter.liljeroth@aalto.fi.

ORCID

Peter Liljeroth: 0000-0003-1253-8097

Author Contributions

‡F.S. and P.H.J. contributed equally.

Notes

The authors declare no competing financial interest.

ACKNOWLEDGMENTS

We thank Kazuto Akagi for his help with the DFT calculations. This research was supported by the European Research Council (ERC-2011-StG No. 278698 "PRECISE-NANO"), the Academy of Finland (Centre of Excellence in Low Temperature Quantum Phenomena and Devices No. 284594), and the Debye Graduate School. This research made use of the Aalto Nanomicroscopy Center (Aalto NMC) facilities.

REFERENCES

(1) Ruffieux, P.; Cai, J.; Plumb, N. C.; Patthey, L.; Prezzi, D.; Ferretti, A.; Molinari, E.; Feng, X.; Müllen, K.; Pignedoli, C. A.; et al. Electronic structure of atomically precise graphene nanoribbons. *ACS Nano* **2012**, *6*, 6930−6935.

(2) Castro Neto, A. H.; Guinea, F.; Peres, N. M. R.; Novoselov, K. S.; Geim, A. K. The electronic properties of graphene. *Rev. Mod. Phys.* **2009**, *81*, 109−162.

(3) Han, M. Y.; Ozyilmaz, B.; Zhang, Y.; Kim, P. Energy band-gap engineering of graphene nanoribbons. *Phys. Rev. Lett.* **2007**, *98*, 206805.

(4) Bai, J.; Duan, X.; Huang, Y. Rational fabrication of graphene nanoribbons using a nanowire etch mask. *Nano Lett.* **2009**, *9*, 2083−2087.

(5) Jiao, L.; Zhang, L.; Wang, X.; Diankov, G.; Dai, H. Narrow graphene nanoribbons from carbon nanotubes. *Nature* **2009**, *458*, 877−880.

(6) Kosynkin, D. V.; Higginbotham, A. L.; Sinitskii, A.; Lomeda, J. R.; Dimiev, A.; Price, B. K.; Tour, J. M. Longitudinal unzipping of carbon nanotubes to form graphene nanoribbons. *Nature* **2009**, *458*, 872−U5.

(7) Yazyev, O. V.; Capaz, R. B.; Louie, S. G. Theory of magnetic edge states in chiral graphene nanoribbons. *Phys. Rev. B: Condens. Matter Mater. Phys.* **2011**, *84*, 115406.

(8) Grill, L.; Dyer, M.; Lafferentz, L.; Persson, M.; Peters, M. V.; Hecht, S. Nano-architectures by covalent assembly of molecular building blocks. *Nat. Nanotechnol.* **2007**, *2*, 687−691.

(9) Cai, J.; Ruffieux, P.; Jaafar, R.; Bieri, M.; Braun, T.; Blankenburg, S.; Muoth, M.; Seitsonen, A. P.; Saleh, M.; Feng, X.; et al. Atomically precise bottom-up fabrication of graphene nanoribbons. *Nature* **2010**, *466*, 470−473.

(10) Ruffieux, P.; Wang, S.; Yang, B.; Sánchez-Sánchez, C.; Liu, J.; Dienel, T.; Talirz, L.; Shinde, P.; Pignedoli, C. A.; Passerone, D.; et al.

DOI: 10.1021/acs.jpcc.6b12428
J. Phys. Chem. C 2017, 121, 2896−2904

On-surface synthesis of graphene nanoribbons with zigzag edge topology. *Nature* **2016**, *531*, 489−492.
(11) Chen, Y.-C.; de Oteyza, D. G.; Pedramrazi, Z.; Chen, C.; Fischer, F. R.; Crommie, M. F. Tuning the band gap of graphene nanoribbons synthesized from molecular precursors. *ACS Nano* **2013**, *7*, 6123−6128.
(12) Nguyen, G. D.; Toma, F. M.; Cao, T.; Pedramrazi, Z.; Chen, C.; Rizzo, D. J.; Joshi, T.; Bronner, C.; Chen, Y.-C.; Favaro, M.; et al. Bottom-up synthesis of N = 13 sulfur-doped graphene nanoribbons. *J. Phys. Chem. C* **2016**, *120*, 2684−2687.
(13) Kawai, S.; Saito, S.; Osumi, S.; Yamaguchi, S.; Foster, A. S.; Spijker, P.; Meyer, E. Atomically controlled substitutional boron-doping of graphene nanoribbons. *Nat. Commun.* **2015**, *6*, 8098.
(14) Cloke, R. R.; Marangoni, T.; Nguyen, G. D.; Joshi, T.; Rizzo, D. J.; Bronner, C.; Cao, T.; Louie, S. G.; Crommie, M. F.; Fischer, F. R. Site-specific substitutional boron doping of semiconducting armchair graphene nanoribbons. *J. Am. Chem. Soc.* **2015**, *137*, 8872−8875.
(15) Bronner, C.; Stremlau, S.; Gille, M.; Brausse, F.; Haase, A.; Hecht, S.; Tegeder, P. Aligning the band gap of graphene nanoribbons by monomer doping. *Angew. Chem., Int. Ed.* **2013**, *52*, 4422−4425.
(16) Cai, J.; Pignedoli, C. A.; Talirz, L.; Ruffieux, P.; Soede, H.; Liang, L.; Meunier, V.; Berger, R.; Li, R.; Feng, X.; et al. Graphene nanoribbon heterojunctions. *Nat. Nanotechnol.* **2014**, *9*, 896−900.
(17) Kimouche, A.; Ervasti, M. M.; Drost, R.; Halonen, S.; Harju, A.; Joensuu, P. M.; Sainio, J.; Liljeroth, P. Ultra-narrow metallic armchair graphene nanoribbons. *Nat. Commun.* **2015**, *6*, 10177.
(18) Zhang, H.; Lin, H.; Sun, K.; Chen, L.; Zagranyarski, Y.; Aghdassi, N.; Duhm, S.; Li, Q.; Zhong, D.; Li, Y.; et al. On-surface synthesis of rylene-type graphene nanoribbons. *J. Am. Chem. Soc.* **2015**, *137*, 4022−4025.
(19) Liu, J.; Li, B.-W.; Tan, Y.-Z.; Giannakopoulos, A.; Sánchez-Sánchez, C.; Beljonne, D.; Ruffieux, P.; Fasel, R.; Feng, X.; Müllen, K. Toward cove-edged low band gap graphene nanoribbons. *J. Am. Chem. Soc.* **2015**, *137*, 6097−6103.
(20) de Oteyza, D. G.; García-Lekue, A.; Vilas-Varela, M.; Merino-Díez, N.; Carbonell-Sanromà, E.; Corso, M.; Vasseur, G.; Rogero, C.; Guitián, E.; Pascual, J. I.; et al. Substrate-independent growth of atomically precise chiral graphene nanoribbons. *ACS Nano* **2016**, *10*, 9000−9008.
(21) Huang, H.; Wei, D.; Sun, J.; Wong, S. L.; Feng, Y. P.; Castro Neto, A. H.; Wee, A. T. S. Spatially resolved electronic structures of atomically precise armchair graphene nanoribbons. *Sci. Rep.* **2012**, *2*, 983.
(22) Ullmann, F.; Bielecki, J. Ueber Synthesen in der Biphenylreihe. *Ber. Dtsch. Chem. Ges.* **1901**, *34*, 2174−2185.
(23) Talirz, L.; Ruffieux, P.; Fasel, R. On-surface synthesis of atomically precise graphene nanoribbons. *Adv. Mater.* **2016**, *28*, 6222−6231.
(24) Björk, J.; Hanke, F.; Stafström, S. Mechanisms of halogen-based covalent self-assembly on metal surfaces. *J. Am. Chem. Soc.* **2013**, *135*, 5768−5775.
(25) Li, X.; Cai, W.; An, J.; Kim, S.; Nah, J.; Yang, D.; Piner, R.; Velamakanni, A.; Jung, I.; Tutuc, E.; et al. Large-area synthesis of high-quality and uniform graphene films on copper foils. *Science* **2009**, *324*, 1312−1314.
(26) Li, X.; Zhu, Y.; Cai, W.; Borysiak, M.; Han, B.; Chen, D.; Piner, R. D.; Colombo, L.; Ruoff, R. S. Transfer of large-area graphene films for high-performance transparent conductive electrodes. *Nano Lett.* **2009**, *9*, 4359−4363.
(27) Bae, S.; Kim, H.; Lee, Y.; Xu, X.; Park, J.-S.; Zheng, Y.; Balakrishnan, J.; Lei, T.; Kim, H. R.; Song, Y. I.; et al. Roll-to-roll production of 30-in. graphene films for transparent electrodes. *Nat. Nanotechnol.* **2010**, *5*, 574−578.
(28) Simonov, K. A.; Vinogradov, N. A.; Vinogradov, A. S.; Generalov, A. V.; Zagrebina, E. M.; Mårtensson, N.; Cafolla, A. A.; Carpy, T.; Cunniffe, J. P.; Preobrajenski, A. B. Effect of substrate chemistry on the bottom-up fabrication of graphene nanoribbons: Combined core-level spectroscopy and STM study. *J. Phys. Chem. C* **2014**, *118*, 12532−12540.
(29) Han, P.; Akagi, K.; Federici Canova, F.; Mutoh, H.; Shiraki, S.; Iwaya, K.; Weiss, P. S.; Asao, N.; Hitosugi, T. Bottom-up graphene-nanoribbon fabrication reveals chiral edges and enantioselectivity. *ACS Nano* **2014**, *8*, 9181−9187.
(30) Simonov, K. A.; Vinogradov, N. A.; Vinogradov, A. S.; Generalov, A. V.; Zagrebina, E. M.; Mårtensson, N.; Cafolla, A. A.; Carpy, T.; Cunniffe, J. P.; Preobrajenski, A. B. Comment on "Bottom-up graphene-nanoribbon fabrication reveals chiral edges and enantioselectivity". *ACS Nano* **2015**, *9*, 3399−3403.
(31) Han, P.; Akagi, K.; Federici Canova, F.; Mutoh, H.; Shiraki, S.; Iwaya, K.; Weiss, P. S.; Asao, N.; Hitosugi, T. Reply to "Comment on 'Bottom-up graphene-nanoribbon fabrication reveals chiral edges and enantio selectivity' ". *ACS Nano* **2015**, *9*, 3404−3405.
(32) Simonov, K. A.; Vinogradov, N. A.; Vinogradov, A. S.; Generalov, A. V.; Zagrebina, E. M.; Svirskiy, G. I.; Cafolla, A. A.; Carpy, T.; Cunniffe, J. P.; Taketsugu, T.; et al. From graphene nanoribbons on Cu(111) to nanographene on Cu(110): Critical role of substrate structure in the bottom-up fabrication strategy. *ACS Nano* **2015**, *9*, 8997−9011.
(33) Han, P.; Akagi, K.; Federici Canova, F.; Shimizu, R.; Oguchi, H.; Shiraki, S.; Weiss, P. S.; Asao, N.; Hitosugi, T. Self-assembly strategy for fabricating connected graphene nanoribbons. *ACS Nano* **2015**, *9*, 12035−12044.
(34) Sánchez-Sánchez, C.; Dienel, T.; Deniz, O.; Ruffieux, P.; Berger, R.; Feng, X.; Müllen, K.; Fasel, R. Purely armchair or partially chiral: Noncontact atomic force microscopy characterization of dibromo-bianthryl-based graphene nanoribbons grown on Cu(111). *ACS Nano* **2016**, *10*, 8006−8011.
(35) Schulz, F.; Hämäläinen, S.; Liljeroth, P. Atomic-scale contrast formation in AFM images on molecular systems In *Noncontact Atomic Force Microscopy*; Morita, S., Giessibl, J. F., Meyer, E., Wiesendanger, R., Eds.; Springer International Publishing: Amsterdam, 2015; Vol. 3, Chapter 10, pp 173−194.
(36) Albrecht, T. R.; Grutter, P.; Horne, D.; Rugar, D. Frequency-modulation detection using high-Q cantilevers for enhanced force microscope sensitivity. *J. Appl. Phys.* **1991**, *69*, 668−673.
(37) Gross, L.; Mohn, F.; Moll, N.; Liljeroth, P.; Meyer, G. The chemical structure of a molecule resolved by atomic force microscopy. *Science* **2009**, *325*, 1110−1114.
(38) van der Lit, J.; Boneschanscher, M. P.; Vanmaekelbergh, D.; Ijäs, M.; Uppstu, A.; Ervasti, M.; Harju, A.; Liljeroth, P.; Swart, I. Suppression of electron-vibron coupling in graphene nanoribbons contacted via a single atom. *Nat. Commun.* **2013**, *4*, 2023.
(39) Dienel, T.; Kawai, S.; Soede, H.; Feng, X.; Müllen, K.; Ruffieux, P.; Fasel, R.; Groening, O. Resolving atomic connectivity in graphene nanostructure junctions. *Nano Lett.* **2015**, *15*, 5185−5190.
(40) Jacobse, P. H.; van den Hoogenband, A.; Moret, M.-E.; Klein Gebbink, R. J. M.; Swart, I. Aryl radical geometry determines nanographene formation on Au(111). *Angew. Chem., Int. Ed.* **2016**, *55*, 13052−13055.
(41) Bartels, L.; Meyer, G.; Rieder, K.-H. Controlled vertical manipulation of single CO molecules with the scanning tunneling microscope: A route to chemical contrast. *Appl. Phys. Lett.* **1997**, *71*, 213−215.
(42) Lippert, G.; Hutter, J.; Parrinello, M. A hybrid Gaussian and plane wave density functional scheme. *Mol. Phys.* **1997**, *92*, 477−487.
(43) VandeVondele, J.; Krack, M.; Mohamed, F.; Parrinello, M.; Chassaing, T.; Hutter, J. Quickstep: Fast and accurate density functional calculations using a mixed Gaussian and plane waves approach. *Comput. Phys. Commun.* **2005**, *167*, 103−128.
(44) Grimme, S. Semiempirical GGA-type density functional constructed with a long-range dispersion correction. *J. Comput. Chem.* **2006**, *27*, 1787−1799.
(45) VandeVondele, J.; Hutter, J. Gaussian basis sets for accurate calculations on molecular systems in gas and condensed phases. *J. Chem. Phys.* **2007**, *127*, 114105.
(46) Hapala, P.; Kichin, G.; Wagner, C.; Tautz, F. S.; Temirov, R.; Jelinek, P. Mechanism of high-resolution STM/AFM imaging with

DOI: 10.1021/acs.jpcc.6b12428
J. Phys. Chem. C 2017, 121, 2896−2904

functionalized tips. *Phys. Rev. B: Condens. Matter Mater. Phys.* **2014**, *90*, 085421.
(47) Hämäläinen, S. K.; van der Heijden, N.; van der Lit, J.; den Hartog, S.; Liljeroth, P.; Swart, I. Intermolecular contrast in atomic force microscopy images without intermolecular bonds. *Phys. Rev. Lett.* **2014**, *113*, 186102.
(48) Tracey, J.; Federici Canova, F.; Keisanen, O.; Gao, D. Z.; Spijker, P.; Reischl, B.; Foster, A. S. Flexible and modular virtual scanning probe microscope. *Comput. Phys. Commun.* **2015**, *196*, 429−438.
(49) Vanommeslaeghe, K.; MacKerell, A. D. Automation of the CHARMM General Force Field (CGenFF) I: Bond perception and atom typing. *J. Chem. Inf. Model.* **2012**, *52*, 3144−3154.
(50) Giessibl, F. J. Advances in atomic force microscopy. *Rev. Mod. Phys.* **2003**, *75*, 949−983.
(51) McMillen, D. F.; Golden, D. M. Hydrocarbon bond-dissociation energies. *Annu. Rev. Phys. Chem.* **1982**, *33*, 493−532.
(52) Shi, K. J.; Yuan, D. W.; Wang, C. X.; Shu, C. H.; Li, D. Y.; Shi, Z. L.; Wu, X. Y.; Liu, P. N. Ullmann reaction of aryl chlorides on various surfaces and the application in stepwise growth of 2D covalent organic frameworks. *Org. Lett.* **2016**, *18*, 1282−1285.
(53) Pavliček, N.; Fleury, B.; Neu, M.; Niedenführ, J.; Herranz-Lancho, C.; Ruben, M.; Repp, J. Atomic force microscopy reveals bistable configurations of dibenzo[a,h]thianthrene and their interconversion pathway. *Phys. Rev. Lett.* **2012**, *108*, 086101.
(54) van der Lit, J.; Jacobse, P. H.; Vanmaekelbergh, D.; Swart, I. Bending and buckling of narrow armchair graphene nanoribbons via STM manipulation. *New J. Phys.* **2015**, *17*, 053013.
(55) Park, J.; Kim, K. Y.; Chung, K.-H.; Yoon, J. K.; Kim, H.; Han, S.; Kahng, S.-J. Interchain interactions mediated by Br adsorbates in arrays of metal-organic hybrid chains on Ag(111). *J. Phys. Chem. C* **2011**, *115*, 14834−14838.
(56) Basagni, A.; Sedona, F.; Pignedoli, C. A.; Cattelan, M.; Nicolas, L.; Casarin, M.; Sambi, M. Molecules-oligomers-nanowires-graphene nanoribbons: A bottom-up stepwise on-surface covalent synthesis preserving long-range order. *J. Am. Chem. Soc.* **2015**, *137*, 1802−1808.
(57) Bieri, M.; Nguyen, M.-T.; Groening, O.; Cai, J.; Treier, M.; Ait-Mansour, K.; Ruffieux, P.; Pignedoli, C. A.; Passerone, D.; Kastler, M.; et al. Two-dimensional polymer formation on surfaces: Insight into the roles of precursor mobility and reactivity. *J. Am. Chem. Soc.* **2010**, *132*, 16669−16676.
(58) Stöckl, Q. S.; Hsieh, Y.-C.; Mairena, A.; Wu, Y.-T.; Ernst, K.-H. Aggregation of C_{70}-fragment buckybowls on surfaces: π-H and π-π bonding in bowl up-side-down ensembles. *J. Am. Chem. Soc.* **2016**, *138*, 6111−6114.

DOI: 10.1021/acs.jpcc.6b12428
J. Phys. Chem. C 2017, 121, 2896−2904